

Resolved Spectroscopy of the Narrow-Line Region in NGC 1068.

II. Physical Conditions Near the NGC 1068 “Hot-Spot”¹

Steven B. Kraemer^{2,3}, & D. Michael Crenshaw^{2,4}

Received _____; accepted _____

¹Based on observations made with the NASA/ESA Hubble Space Telescope. STScI is operated by the Association of Universities for Research in Astronomy, Inc. under the NASA contract NAS5-26555.

²Catholic University of America, NASA/Goddard Space Flight Center, Code 681, Greenbelt, MD 20771.

³Email: stiskraemer@yancey.gsfc.nasa.gov.

⁴Email: crenshaw@buckeye.gsfc.nasa.gov.

ABSTRACT

The physical conditions near the optical continuum peak (“hot spot”) in the inner narrow line region (NLR) of the Seyfert 2 galaxy, NGC 1068, are examined using ultraviolet and optical spectra and photoionization models. The spectra were taken with the *Hubble Space Telescope*/Space Telescope Imaging Spectrograph (*HST*/STIS), through the $0''.1 \times 52''.0$ slit, covering the full STIS 1200 Å to 10000 Å waveband, and are from a region that includes the hot spot, extending $0''.2$, or ~ 14 pc (for $H_0 = 75 \text{ km sec}^{-1} \text{ Mpc}^{-1}$), in the cross-dispersion direction. The spectra show emission-lines from a wide range of ionization states for the most abundant elements, similar to archival Faint Object Spectrograph spectra of the same region. Perhaps the most striking feature of these spectra is the presence of strong coronal emission lines, including [S XII] $\lambda 7611$ which has hitherto only been identified in spectra of the solar corona. There is an apparent correlation between ionization energy and velocity of the emission lines with respect to the systemic velocity of the host galaxy, with the coronal lines blueshifted, most other high excitation lines near systemic, and some of the low ionization lines redshifted. From the results of our modeling, we find that the emission-line gas is photoionized and consists of three principal components: 1) one in which most of the strong emission-lines, such as [O III] $\lambda 5007$, [Ne V] $\lambda 3426$, C IV $\lambda 1550$, arise, 2) a more tenuous, highly ionized component, which is the source of the coronal-line emission, and 3) a component, which is not co-planar with the other two, in which the low ionization and neutral lines, such as [N II] $\lambda 6548$ and [O I] $\lambda 6300$, are formed. The first two components are directly ionized by the EUV-Xray continuum emitted by the central source, while the low ionization gas is ionized by a combination of highly absorbed continuum radiation and a small fraction of unabsorbed continuum scattered by

free electrons associated with the hot spot. The combination of covering factor and Thomson optical depth of the high ionization components is insufficient to scatter the observed fraction of continuum radiation into our line-of-sight. Therefore, the scattering must occur in an additional component of hot plasma, which contributes little or no UV/optical line emission.

Subject headings: galaxies: individual (NGC 1068) – galaxies: Seyfert

1. Introduction

NGC 1068, one of the initial set of emission line galaxies studied by Seyfert (1943), is the nearest ($z=0.0038$) and best studied of the Seyfert 2 galaxies. Based on the widths of their emission lines in optical spectra, Seyfert galaxies are generally divided into two types (Khachikian & Weedman 1971). Seyfert 1s possess broad permitted lines, with full widths at half maximum (FWHM) $\geq 10^3 \text{ km s}^{-1}$, and narrower forbidden lines, with FWHM $\approx 500 \text{ km s}^{-1}$, while Seyfert 2s show only narrow emission lines. The optical continua of Seyfert 1 galaxies are dominated by nonstellar emission that can be characterized by a power-law (Oke & Sargent 1968), whereas this component is much weaker in Seyfert 2 galaxies (Koski 1978). Spectropolarimetric studies (Miller & Antonucci 1983; Antonucci & Miller 1985) revealed the presence of strongly polarized continuum and broad permitted line emission within a $3''.0$ aperture centered on the optical nucleus of NGC 1068. These observations were the inspiration for the unified model for Seyfert galaxies, according to which the differences between types 1 and 2 are due to viewing angle, with Seyfert 2 galaxies characterized by obscuration of their broad-line regions and central engines (cf. Antonucci 1994). The polarization is wavelength independent, which implies that the emission from the hidden continuum source and broad-line region is scattered into our line-of-sight by free electrons within a hot ($\sim 3 \times 10^5 \text{ K}$) plasma in the inner Narrow-Line Region (NLR) (Miller, Goodrich, & Mathews 1991).

The structure of the nuclear region has been observed extensively with *HST*, using the Planetary Camera (pre-COSTAR; Lynds et al. 1991), and the Faint Object Camera (Capetti et al. 1995). The peak in the optical continuum is resolved, with a FWHM of approximately $0''.15$, roughly centered within a cloud of dimensions $3''.5 \times 1''.7$ elongated in the NE-SW direction, the latter consisting primarily of starlight (Lynds et al. 1991; Crenshaw & Kraemer 1999, hereafter Paper I). The NE part of the cloud has the physical

dimensions and location attributed to the scattering medium modeled by Miller, et al. (1991), which has been revealed in the UV (Kriss et al. 1993; Macchetto et al. 1994) and which we have discussed in detail in Paper I. A bright knot of [O III] $\lambda 5007$ emission, often referred to as Cloud B (Evans et al. 1991), overlaps the continuum emission from the hot spot; its centroid is $\sim 0''.2$ north of that of the hot spot.

While Cloud B lies close to the apex of emission-line bicone (Evans et al. 1991), there is evidence that the actual hidden nucleus is further to the south and west (Capetti, Macchetto, & Lattanzi 1997). It has been suggested that a thermal radio source, S1, $0''.3$ south of the continuum peak, is the true nucleus (Evans et al. 1991; Gallimore et al 1997). The discovery of an H₂O megamaser with a velocity width of 600 km s^{-1} (Claussen & Lo 1986) associated with S1 (cf. Greenhill & Gwinn 1997), is further evidence that S1 is the nucleus. Even so, the optical continuum peak and a portion of Cloud B are within 30 pc of the nucleus, and therefore exposed to an intense flux of ionizing radiation.

Coronal iron lines have been detected in a number of Seyfert galaxies (Grandi 1978; Osterbrock 1981; Penston et al. 1984; Osterbrock 1985). The following coronal-lines are known to be present in the spectrum of NGC 1068: [Fe X] $\lambda 6374$ (Koski 1976), [Fe XI] $\lambda 7892$ (Penston et al. 1984; Osterbrock & Fulbright 1996), and [Si X] $1.430 \mu\text{m}$ (Thompson 1996). It has been recently suggested (Reynolds et al. 1997) that the coronal-line emission arises in the outer regions of the X-ray absorber present in many Seyfert galaxies (see Reynolds (1997) and George et al. (1998) for a discussion of the properties of X-ray absorbers). Furthermore, Krolik & Kriss (1995) have postulated that the scattering medium in Seyfert 2 galaxies may be the same gas that produces the X-ray absorption in Seyfert 1s. Providing better constraints on the physical conditions in the gas in which the coronal lines arise will help in understanding the connection between the emission-line gas and the scattering medium and, possibly, the X-ray absorber.

In this paper we will examine the physical conditions near Cloud B and the optical hot spot in the nucleus of NGC 1068. Among our results, we report the presence of the highest ionization energy UV/optical lines ever detected in a Seyfert 2 galaxy. In Section 3 we will discuss the observed relationship between ionization potential and the velocity of the emission-lines with respect to the systemic velocity of the host galaxy. In Sections 4 and 5 we will present the details of photoionization models of the emission-line gas. Finally we will discuss the relation between the emission-line gas, the scattering of the continuum radiation, and the structure of the inner NLR.

2. Observations and Analysis

We obtained STIS long-slit spectra of NGC 1068 over $1150 - 10,270 \text{ \AA}$ on 1998 August 15. Paper I shows the slit position and describes the observations and data reduction. The spectra that are analyzed in this paper are from the central $0''.2 \times 0''.1$ bin in Paper I, which includes the brightest portion of the hot spot in our slit and a portion of knot B south of its centroid. We measured the fluxes of most of the narrow emission lines by direct integration over a local baseline determined by linear interpolation between adjacent continuum regions. For severely blended lines such as $H\alpha$ and $[\text{N II}] \lambda\lambda 6548, 6584$, we used the $[\text{O III}] \lambda 5007$ profile as a template to deblend the lines (see Crenshaw & Peterson 1986). We then determined the reddening of the narrow emission lines from the observed $\text{He II } \lambda 1640/\lambda 4686$ ratio, the Galactic reddening curve of Savage & Mathis (1979), and an intrinsic He II ratio of 7.2, which is expected from recombination (Seaton 1978) at the temperatures and densities typical of the NLR (see also Section 4). We determined errors in the dereddened ratios from the sum in quadrature of the errors from three sources: photon noise, different reasonable continuum placements, and reddening.

Table 1 gives the observed and dereddened narrow-line ratios, relative to $H\beta$, and

errors in the dereddened ratios for each position. At the end of the table, we give the $H\beta$ flux ($\text{ergs s}^{-1} \text{cm}^{-2}$) in the bin and the reddening value that we determined from the He II ratios.

3. Spectral Properties of the Gas Near the Hot Spot

Figure 1 shows the UV and optical spectra of the continuum hot spot in NGC 1068. Emission lines are present from a wide range in ionization state for the most numerous elements, such as strong [N II] $\lambda\lambda 6548, 6484$ and N V $\lambda 1240$, and emission lines from the first four ionization states of oxygen, as seen in the earlier FOS spectra (Kraemer, Ruiz, & Crenshaw; hereafter KRC). The continuum shows no strong evidence of a stellar component, and is clearly the result of scattered continuum radiation from the hidden central source, as we discussed in Paper I. Also, the strongest permitted lines show broad wings, which is due to reflected broad-line emission.

Netzer (1997) attributed the apparent weakness of O III] $\lambda 1663$ in the FOS spectra of NGC 1068 to an underabundance of oxygen. On the other hand, we used the ratio of N III] $\lambda 1750$ /O III] $\lambda 1663$ as evidence of an overabundance of nitrogen (KRC). However, it is clear from these STIS data that O III] $\lambda 1663$ has been absorbed by Galactic Al II $\lambda 1671$ (see Figure 1) and, therefore, cannot be used to estimate either the O/H or N/O abundance ratios.

The most intriguing feature of these spectra, which was not readily apparent in the FOS data, is the presence of a number of coronal lines, including those from extremely high ionization states. As shown in Table 1, we have confirmed the presence of [Fe X] $\lambda 6374$ and [Fe XI] $\lambda 7892$, which had been previously detected, as noted in Section 1. Furthermore, we have unambiguously detected [Fe XIV] $\lambda 5303$ (see Figure 1), which previously had only

been confirmed to be present in the spectra of the Seyfert 1 galaxies III Zw 77 (Osterbrock 1981) and MCG -6-30-15 (Reynolds et al. 1997) and, possibly, the Seyfert 2 galaxy Tololo 0109 -383 (Fosbury & Samsom 1983; Durret & Bergeron 1988). Perhaps more unexpected is the presence of [S XII] $\lambda 7611$ (see Figure 1). S^{+10} has an ionization energy of 504.7 eV, which makes this highest ionization line ever detected in the spectrum of a Seyfert galaxy, outside the X-ray region, and certainly the highest ever seen in the NLR, besting [Si X] $1.43 \mu\text{m}$, which has an ionization energy of 401.4 eV (Thompson 1996). Since 7611 \AA is within one of the O_2 telluric bands, detection is difficult from the ground. In fact, the only *confirmed* detection of [S XII] has been in observations of the solar corona during the total eclipse of 30 May 1965 (Jefferies, Orrall, & Zirker 1971). Osterbrock (1981) detected a line at a measured wavelength of 7613.1 \AA in the spectrum of III Zw 77, but did not identify it; we would suggest that this is also [S XII].

In addition to the above-mentioned lines, we have identified a number of other coronal lines in these spectra, as indicated by the ionization potentials listed in Table 1 (for the purposes of this paper, we refer to ions with ionization energies greater than 100 eV as “coronal”; this leaves out the [Ne V] and [Fe VII] lines, which, although detected in the solar corona, are formed under more typical NLR conditions). To our knowledge, these other lines have not been previously identified in the spectra of Seyfert galaxies, although we would expect that they should be present, since their ionization energies are lower than that of Fe^{+13} . Exceptions, perhaps, are the tentatively identified nickel lines, [Ni XV] $\lambda 6702$ and [Ni XIII] $\lambda 5116$, since the other lines are from more abundant elements. However, Halpern & Oke (1986) detected [Ni II] $\lambda 7378$ in an off-nuclear spectrum of NGC 1068, and determined that the nickel abundance may be at least 4 times solar. One of the interesting aspects of the coronal lines is that they are blueshifted with respect to the lower ionization lines, an effect first noted in a number of Seyfert galaxies by Penston et al. (1984). In Figure 2, we plot ionization potential versus recession velocity (cz) for all the observed emission

lines. Note that the presence of a blueshifted absorption feature can bias the centroiding of the line redward, as appears to be the case for N V $\lambda 1240$ and C IV $\lambda 1550$ (KRC). Similarly, the velocity measurement is more difficult for severely blended lines. Nevertheless, there is a strong correlation between ionization potential and velocity. A simple explanation is that the lines originate in different regions that are superimposed, such that we are viewing components with different velocities along our line-of-sight. Note that most of the lower ionization lines are redshifted with respect to the systemic velocity of the host galaxy.

Figure 3 shows spatial cross-cut profiles of the [Fe XIV] $\lambda 5303$ and [S XII] $\lambda 7611$ lines, along the slit. Clearly, the coronal line emission is concentrated directly on the optical hot spot, in contrast to the suggestion that it extends throughout the NLR in Seyfert galaxies (Korista & Ferland 1989), but in general agreement with Penston et al. (1984) regarding the origin of the [Fe X] $\lambda 6374$ and [Fe XI] $\lambda 7892$ lines, and results from line profile studies (cf. Moore, Cohen, & Marcy 1996). Furthermore, the coronal line emission is clumpier and not as extended as the continuum radiation. Of particular interest is the region NE of the hot spot, where the scattered continuum is strongest (see Paper I). This does not necessarily mean that the coronal lines cannot arise in the same gas that scatters the continuum radiation, but, if they do, conditions in the scatterer must vary such that the lines are often weak. The possible connection between the scatterer and the coronal gas is discussed in Section 7.1.

4. Photoionization Models

4.1. Abundances and Ionizing Continuum

Our approach in photoionization modeling of NGC 1068 was described in detail in KRC. We will not repeat the details in the current paper, except to point out important

differences. As usual, the models are parameterized in terms of the dimensionless ionization parameter, U , which is the number of ionizing photons per hydrogen atom at the illuminated face of the cloud. Since the lines of Ne^{+4} and Fe^{+6} are quite strong in the spectrum of NGC 1068, we had assumed that this is in part due to an overabundance of these elements relative to solar (cf. Oliva 1997). We still consider this to be true for iron, since *ASCA* data indicate a large Fe/O ratio in the X-ray emitting gas (Netzer & Turner 1997). However, there is reason to believe that the Ne/H ratio is not substantially greater than solar at least in the extreme inner NLR. The strength of the [Ne V] $\lambda 3426$ relative to hydrogen is sensitive to the optical thickness of the emission-line gas. That is, if a cloud does not extend much beyond the He^{++} zone, [Ne V] $\lambda 3426/\text{H}\beta$ can be quite large (~ 5). Also, if the ionizing continuum is somewhat harder than we had assumed, there are more photons capable of ionizing Ne^{+3} .

In KRC, we had made the argument for a supersolar abundance of nitrogen in the inner NLR of NGC 1068, based on the strength of N V $\lambda 1240$ relative to He II $\lambda 1640$ and C IV $\lambda 1550$ (cf. Ferland et al. 1996). However, the models significantly overpredicted N IV] $\lambda 1486$, which might indicate that that we overestimated the nitrogen abundance. The relative strength of N V $\lambda 1240$, and other resonance lines, can be boosted somewhat by fluorescence and scattering of ultraviolet continuum radiation from the central source (cf. Grandi 1975a, b). As we will discuss in Section 6.1, continuum scattering and fluorescence cannot fully explain the strength of N V $\lambda 1240$. However, based on the observed N IV] $\lambda 1486/\text{H}\beta$ ratio, there is no reason to believe that the relative abundance of nitrogen is significantly greater than solar.

Thus, other than iron, we have chosen to assume solar abundances (cf. Grevesse & Anders 1989) for these models. The numerical abundances, relative to hydrogen, are as follows: He=0.1, C= 3.4×10^{-4} , O= 6.8×10^{-4} , N= 1.2×10^{-4} , Ne= 1.1×10^{-4} , S= 1.5×10^{-5} ,

Si=3.1x10⁻⁵, Mg=3.3x10⁻⁵, Fe=8.0x10⁻⁵.

In KRC, we assumed an ionizing continuum similar to that proposed by Pier et al. (1994), which is a conservative power-law fit from the UV and to the X-ray, using the 2 keV flux and X-ray continuum derived from the BBXRT data (Marshall et al. 1993). However, fits to the X-ray continuum by combining *ROSAT*/PSPC and *Ginga*, or *Einstein*/IPC and *EXOSAT* data (see Pier et al. 1994, and references therein) are consistent with a somewhat harder spectral energy distribution (SED). As noted above, the strength of [Ne V] λ 3426 depends on the hardness of the ionizing continuum. Therefore, we modeled the SED as a broken power-law of the form, $F_\nu = K\nu^{-\alpha}$, as follows:

$$\alpha = 1.0, \quad h\nu < 13.6eV \quad (1)$$

$$\alpha = 1.4, \quad 13.6eV \leq h\nu < 1000eV \quad (2)$$

$$\alpha = 0.5, \quad h\nu \geq 1000eV \quad (3)$$

Note that we have assumed a harder EUV - Xray continuum than in KRC (1.4, rather than 1.6) and have positioned the X-ray break at one-half the energy. We have, however, assumed the same intrinsic luminosity above the Lyman limit, $Q = 4 \times 10^{54}$ photons sec⁻¹ (Pier et al. 1994), which is typical of Seyfert 1 nuclei .

4.2. Component Parameters

As noted in Section 3, these spectra show emission from a wide range of ionization states, which is an indication that we are seeing emission from a range of physical conditions. Also, there is an apparent correlation between the redshift of the emission lines and the ionization potential of the ion from which they arise. Thus, it is likely that we are observing emission from several distinct components.

An initial guess at temperature and density of much of the emission-line gas (which we will refer to as the HIGHION component) can be derived from the ratio of [O III] $\lambda\lambda 5007, 4959$ /[O III] $\lambda 4363$ (Osterbrock 1989). The dereddened observed ratio is ~ 47 , indicating an electron temperature $T_e \leq 20,000\text{K}$ in the low density limit, and little modification by collisional de-excitation of the 1D_2 level. [Fe VII] lines ratios can also be used to estimate temperature. The ratio [Fe VII] $\lambda 3759$ /[Fe VII] $\lambda 6087 \approx 0.79$, which indicates $T_e \sim 25,000\text{K}$, at electron densities, $n_e, \leq 10^6 \text{ cm}^{-3}$ (Nussbaumer & Storey 1982). Still, it is possible that much of the [Fe VII] and [O III] emission arises in different zones within the same gas, particularly since these lines are at the same approximate velocity (see Table 1).

If one kinematic component contributes most of the [O III] and [Fe VII] emission, and presumably other lines within the same range of ionization energy (see Table 1), it is not likely to contribute the highest ionization lines in these spectra. As we discussed in Section 3, such lines as [Fe IX] $\lambda 7892$, [Fe XIV] $\lambda 5303$, and [S XII] $\lambda 7611$, are blueshifted with respect to the lower ionization lines by several hundred km sec^{-1} , which suggests that they arise in a different kinematic component (which we will refer to as CORONAL). It has been previously suggested that a rough estimate of the temperature of the coronal gas can be obtained from the ratio of [Fe XI] $\lambda 2649$ /[Fe XI] $\lambda 7892$ (Penston et al. 1984; Osterbrock & Fulbright 1996). The observed ratio is [Fe XI] $\lambda 2649$ /[Fe XI] $\lambda 7892 = 1.4^{+.43}_{-.35}$. Unfortunately, based on the most recent calculations for effective collision strengths (Tayal 1999), this ratio is not particularly sensitive to temperature at electron densities $\leq 10^8 \text{ cm}^{-3}$. Using these collision strengths and the transition probabilities from Mason (1975), the dereddened [Fe XI] ratio indicates that $T_e > 3 \times 10^4 \text{ K}$ in the Fe^{+10} zone. Since the redshifts of the Balmer lines are similar to those of the [O III] lines, we expect CORONAL will contribute little to the total hydrogen recombination line flux.

Since the lowest ionization lines appear redshifted compared to the other emission-lines, it is probable that they arise in a separate component, rather than in the more neutral parts of HIGHION. This component must be of fairly low density, since the ratio of [S II] $\lambda 6716$ /[S II] $\lambda 6731 \approx 0.81$, indicating $n_e \sim 2 \times 10^3 \text{ cm}^{-2}$ (Osterbrock 1989). The S⁺ lines can arise in partially neutral gas and, thus, we estimate that the atomic hydrogen density for this component is somewhat higher, $n_H \leq$ a few times 10^4 cm^{-2} . The nature of such a component (which we will refer to as LOWION) was discussed extensively in KRC. The fact that the strengths of the low-ionization, collisionally-excited lines must be large relative to the Balmer lines in order for them to appear strong in a composite spectrum led us to believe that the gas was screened and, thus, ionized by an absorbed continuum strongly weighted to the X-ray (KRC). However, the paucity of ionizing photons in the absorbed continuum and the constraint that this component had the same covering factor as the screening gas led to an underprediction of its contribution to the total emission-line flux. In these spectra it is apparent that much of the high ionization gas is optically thin, since the observed He II $\lambda 4686$ /H β ratio is 0.60, which is unattainable if much of the gas is optically thick near the Lyman limit. Thus, neither of the other components can provide an effective screen for LOWION.

Kraemer et al. (1999a) have modeled the effect on the NLR of an absorber with a high covering factor within a few parsecs of the continuum source, and this effect is clearly evident in the NLR spectrum of NGC 4151 (Alexander et al. 1999; Kraemer et al 1999b). Thus, we suggest the following geometry for the inner NLR of NGC 1068. The components represented by HIGHION and CORONAL are essentially co-located, and are ionized by unabsorbed continuum radiation from the hidden nucleus. The low ionization gas lies out of the plane occupied by HIGHION and CORONAL, and is irradiated by X-rays which penetrate a layer of absorbing gas closer to the nucleus. Also a small fraction of unabsorbed continuum, scattered out of the plane by free electrons, is incident upon the low ionization

gas. This simple geometry is illustrated in Figure 4. There is no simple way to quantify the fractions of scattered and direct continuum irradiating LOWION, but it is thought that at least 1% of the continuum radiation in NGC 1068 is scattered into our line of sight (Miller et al. 1991) and there is the example of a large column, X-ray absorber in NGC 4151 (cf. Barr et al. 1977) which may vary in optical depth as a function of angle with respect to the ionization cone (Kraemer et al. 1999b). We have modeled the absorber assuming an ionization parameter, $U = 0.1$, and a column density, $N_H = 7.4 \times 10^{22} \text{ cm}^{-2}$, where N_H is the sum of the columns of ionized and neutral hydrogen. These parameters are similar to those describing the X-ray absorber in NGC 4151 (Yaqoob, Warwick & Pounds 1989; Weaver et al. 1994). Given our estimate of the luminosity of the active nucleus, an absorber of density $n_H = 10^7 \text{ cm}^{-3}$ would lie at a distance of $\sim 1 \text{ pc}$ from the central engine, closer to the nucleus than the inner part of hot spot. The ionizing continuum incident upon LOWION is shown in Figure 5. For the purposes of these models, we assume that HIGHION and LOWION are at the same radial distance from the nucleus.

Based upon the observed physical properties derived from the emission-lines and the simple geometric picture discussed above, we have generated a three-component photoionization model to describe the physical conditions of line emitting gas. Most of the emission arises in the component HIGHION, with $n_H = 6 \times 10^4 \text{ cm}^{-2}$, $U = 10^{-1.52}$, and $N_H = 10^{21} \text{ cm}^{-2}$. The ionization parameter was chosen to produce strong [Fe VII] emission with negligible [Fe XI] $\lambda 7892$. The model was truncated at the termination of the He^{+2} zone, in order to produce the large He II $\lambda 4686/\text{H}\beta$ ratio and strong [Ne V] described above. The density was constrained on the high end by the presence of strong [Ne IV] $\lambda 2423$, which has a critical density $\sim 10^5 \text{ cm}^{-3}$, and on the low end by the ionization parameter. LOWION is characterized by $n_H = 3 \times 10^4 \text{ cm}^{-2}$, $U = 10^{-3.2}$ (from the combined continuum). Since the size of the partially neutral zone in X-ray ionized gas can be inordinately large, we chose to truncate the model at the same column density as HIGHION. Although not

completely radiation bounded, LOWION has a considerable extended zone behind the H^+/H^0 boundary, from which [O I] $\lambda\lambda 6300, 6364$, Mg II $\lambda 2800$, and [S II] $\lambda\lambda 6716, 6731$ arise. For LOWION, we used a solar iron abundance, since the enhanced cooling by [Fe II] in the extended zone would suppress other lines. The lack of reliable atomic constants for coronal gas at nebular temperatures (i.e., $T_e \leq 10^5\text{K}$) makes it difficult to set the model input parameters for CORONAL on the basis of emission-line ratios. We have generated this component using CLOUDY90 (Ferland et al 1998) since it includes more a complete model for the coronal-line emission, and includes elements, specifically argon and nickel, which are not included in our code. Therefore, we generated a single coronal component to produce the mix of ionization states observed in the blue-shifted emission-lines, assuming the following: $n_H = 7 \times 10^2 \text{ cm}^{-3}$, $U = 1.7$, $N_H = 4 \times 10^{22} \text{ cm}^{-2}$.

In Table 1, the dereddened $L\alpha/H\beta$ is 30.75, which is roughly equal to the value from recombination plus collisional excitation in low ionization gas (Osterbrock 1989). Thus, there is no evidence for the destruction of trapped $L\alpha$ photons by dust. Furthermore, dust is not responsible for scattering of continuum radiation by the hot spot (see Paper I), which is another indication of the absence of dust in this region. Therefore, we have assumed that the emission-line gas is dust-free.

5. Model Results

In creating a composite model, we first scaled the contributions from HIGHION to provide a rough fit to the high ionization lines such as C IV $\lambda 1550$, [Ne V] $\lambda 3426$, and [Fe VII] $\lambda 6087$ and LOWION to fit lines such as [N II] $\lambda 6584$, [O II] $\lambda 3727$, with the result that the contribution of HIGHION to the total $H\beta$ flux is 3 times that of LOWION. Due to the uncertainties in the atomic data, we have elected not to include the predicted forbidden line strengths from CORONAL in our scaling. Since the Balmer lines are associated

kinematically with the non-coronal emission lines, it seems reasonable to expect that the contribution from CORONAL is $\leq 15\%$ of the total $H\beta$ flux, which is only slightly more than the uncertainty in measurement.

In Table 2, we compare the predicted line ratios for HIGHION and LOWION and the composite model to the observed/dereddened values. Given the simplicity of the model, we have obtained very satisfactory fits for the vast majority of the observed emission lines. There is good agreement over nearly the full ionization sequence, for example C IV $\lambda 1550$, C III] $\lambda 1909$, and C II] $\lambda 2325$, and O IV] $\lambda 1402$, [O III] $\lambda 5007$, [O II] $\lambda 3727$, and [O I] $\lambda 6300$. The predicted [O III] $\lambda\lambda 5007, 4959$ /[O III] $\lambda 4363$ ratio is 46, which indicates that T_e in the O^{+2} , averaged over the two components, is correct. The [Fe VII] $\lambda 3759$ /[Fe VII] $\lambda 6087$ ratio is 0.55, lower than the observed value, which indicates a somewhat higher temperature in the Fe^{+6} zone than predicted, which is not surprising since given our model requirement that this zone is co-located with the O^{+2} zone. The predicted [S II] $\lambda 6716/\lambda 6731$ ratio is 1.15, identical to that observed within the errors, which confirms our assumptions regarding the density and ionization structure of LOWION. In general, the model predictions demonstrate that our assumptions regarding the elemental abundances are approximately correct. However, the models do underpredict the strengths of the neon lines somewhat, which may indicate that the neon is supersolar, but probably less than a factor of two.

The model prediction for the He II $\lambda 4686/H\beta$ and ratio is only slightly higher than observed. The predicted strengths of the lines formed in the partially neutral envelope of the low ionization gas, such as [S II] $\lambda\lambda 6716, 6731$ and [O I] $\lambda 6300$, are in reasonable agreement with the observations. This indicates that the combined effects of SED and column density are well represented by the models. This result is of particular importance, given the assumption that the components are ionized by different continua.

Also listed in Table 2 are the model predictions for the emitted $H\beta$ flux, the emitting surface area (the scaled to the reddening-corrected $H\beta$ luminosity divided by the emitted flux), and covering factor for each component, assuming a distance of ~ 25 pc from the hidden continuum source. At the distance of NGC 1068 (14.4 Mpc, Bland-Hawthorne 1997), the $0''.1$ slit width corresponds to 7.2 pc, yielding a covering factor for the slit of ~ 0.05 . Since the covering factor of these components are substantially lower than 0.05, there is no evidence that we are seeing substantial effects of superimposition of clouds along our line-of-sight.

Our photoionization code does not include pumping of UV resonance lines by scattering of continuum radiation and continuum fluorescence (cf. Ferguson, Ferland, & Pradhan 1994), which may explain the underpredictions of the strengths of several UV resonance lines, including N V $\lambda 1240$, C II $\lambda 1335$ and Mg II $\lambda 2800$. Therefore, we recomputed the LOWION model using CLOUDY90, assuming a turbulent velocity of 50 km s^{-1} . Although pumping of UV resonance lines is most efficient for gas with large turbulent velocities ($\geq 1000 \text{ km s}^{-1}$; Ferguson et al. 1994), it can still be an important process if the covering factor of the emitting gas is sufficiently large (cf. Hamann & Korista 1996) and/or if the optical depths of the scattered lines are small (Ferland 1992). We derive a relatively large covering factor for LOWION ($\sim 20\%$ that of the slit), and thus it is not surprising that the model predicts a significant contribution to resonance lines from scattered continuum radiation (interestingly, this is all due to direct pumping of the UV resonance line, since there is insufficient ionizing radiation incident upon LOWION to pump the EUV driver lines). The CLOUDY90 predictions for C II $\lambda 1335$ and Mg II $\lambda 2800$ are listed in Table 2, alongside those from our code (the predictions for the non-resonance lines were quite similar for the two codes), and the agreement with observed flux ratios is quite good. In addition to the large column densities of C^+ ($3.22 \times 10^{17} \text{ cm}^{-2}$) and Mg^+ ($1.54 \times 10^{16} \text{ cm}^{-2}$), LOWION predicts a large column density for O^0 ($6.02 \times 10^{17} \text{ cm}^{-2}$). O I $\lambda 1302$ is present in the

far-UV spectrum (see Figure 1) and we expect that is also formed by continuum scattering (unfortunately, it is not included in the code output). However, continuum scattering does not appear to have a similarly strong affect in boosting the N V $\lambda 1240$ line, as we discuss below.

In Table 3, we list the predictions of the CORONAL model for the mean ionization fractions; ions with observed lines are flagged. We elected not to list the predicted emission-line ratios since they may be misleading given the lack of reliable atomic data (cf. Moorwood et al. 1997). The model predicts non-negligible populations for each of the observed ionic states, except Si^{+6} and Fe^{+6} , however it is clear that the [Fe VII] lines arise in lower ionization gas. If we assume that CORONAL contributes 15% of the observed $\text{H}\beta$ flux, the covering factor is 2.2×10^{-3} . Assuming isotropic scattering, at small electron scattering optical depths, $\tau_{electron} < 1$, the reflected fraction of continuum radiation, $f_{refl} \approx N_e F_c \sigma_{Thomson}$, where N_e is the column density of electrons, F_c is the covering factor, and $\sigma_{Thomson}$ is the Thomson cross-section. For CORONAL, $f_{refl} \approx 7.4 \times 10^{-5}$. However, the observed reflected continuum fraction in our spectrum, based on the estimated central source luminosity (Pier et al. 1994), is $f_{refl} \sim 1.4 \times 10^{-3}$ (the total reflected fraction is $f_{refl} \approx 1.5 \times 10^{-2}$, consistent with the larger region sampled; Miller et al. 1991). Thus, the coronal-line emitting gas near the hot spot makes a negligible contribution to the scattered continuum radiation.

6. Open Issues

6.1. The Nitrogen Problem

In KRC, we attributed the unusual strength of the N V $\lambda 1240$ line to an overabundance of nitrogen, however, the models significantly overpredicted N IV] $\lambda 1486$. Even with solar

nitrogen abundance, HIGHION overpredicts N IV] $\lambda 1486$ by a factor of nearly 3. A check of HIGHION using CLOUDY90, assuming a turbulent velocity of 500 km s^{-1} , produced only a 70% increase in the strength of N V $\lambda 1240$. The models do not significantly underpredict other lines formed in the same zone as N V $\lambda 1240$, such as [Ne V] $\lambda 3426$ and [Fe VII] $\lambda 6087$, and the predictions for other UV resonance lines match the data or are well understood (see above). One possible explanation is that N V $\lambda 1240$ and N IV] $\lambda 1486$ are formed in different regions, with much different nitrogen abundances, but we find no evidence for abundance inhomogeneities for elements other than iron. Therefore, the problem with the nitrogen lines remains unresolved.

6.2. Coronal Component

The predicted temperatures for CORONAL ($T_e = 9.29 \times 10^4 \text{ K}$ at the ionized face, $3.67 \times 10^4 \text{ K}$ at the point of truncation), are within the range expected from the [Fe XI] $\lambda 2649/\lambda 7892$ ratio. However, since the [Fe XI] ratio is not particularly sensitive to temperature at low density, the estimate of the coronal gas temperature is not well constrained. Hopefully, better estimates may be obtained once more accurate collision strengths are calculated for other coronal lines in the temperature range $10^4 - 10^5 \text{ K}$. In any case, it is clear from our model predictions that the observed ionic states can co-exist in photoionized gas characterized by a single ionization parameter.

7. Discussion

7.1. Coronal Gas, the Scattering Medium, and X-ray Absorbers

As we have demonstrated, the ionic states indicated by the coronal emission-lines can co-exist in a large column of highly ionized gas. The ionization parameter, $U = 1.7$,

is characteristic of the X-ray absorbers present in many Seyfert 1 galaxies (cf. Reynolds 1997). It is tempting to associate the coronal-line emitting gas with the X-ray absorber, as Reynolds et al. (1997) has done for the case of the Seyfert 1 galaxy, MCG -6-30-15. Based on the fraction of Seyfert 1s that possess an X-ray absorber, it is likely that the covering factor of the absorber is 0.5 – 1 (cf. George et al. 1998). However, we find that the covering factor of the coronal-line gas in NGC 1068 is quite low, and thus different from typical X-ray absorbers.

The low covering factor of the coronal gas also makes it unlikely to be the continuum scattering region. Furthermore, Miller et al. (1991) estimated a temperature for the scattering medium, $T_e \sim 3 \times 10^5$ K, which is significantly greater than our model predictions. Therefore, it is likely that the scattering occurs in a component of gas associated with the hot spot that is more highly ionized than our coronal component. If we use the initial conditions, $n_H = 200 \text{ cm}^{-3}$, $U = 8$, and $N_H \sim 10^{22} \text{ cm}^{-2}$, CLOUDY90 predicts a mean $T_e \sim 4.5 \times 10^5$ K, which is close to Miller et al.’s value. If we, again, apply the constraint that this additional component contributes $\leq 15\%$ of the total $H\beta$, the covering factor for this component is ≤ 0.07 and, thus, $f_{refl} \leq 1.2 \times 10^{-3}$, or approximately 85% that observed. We would expect to see some line emission from this component, but only from the most highly ionized species, such as [S XII] $\lambda 7611$. The covering factor for this component is slightly greater than that constrained by the slit width, which would not be surprising if the scatterer is indeed an X-ray absorber viewed across our line-of-sight, as suggested by Krolik & Kriss (1995), and there was some superposition of clouds.

To summarize, we think it is unlikely that the coronal-line gas has a sufficient covering factor to produce the scattered continuum radiation. It is plausible that the scattering occurs in a component of more highly ionized gas, with a high covering factor, which may contribute a fraction of the coronal-line emission. Although the physical conditions of both

components are within the range observed for X-ray absorbers (cf. Reynolds 1997), we suggest that while the absorber may be associated with the scatterer, neither are associated with the coronal-line gas that we observe.

7.2. Photoionization versus Collisional Processes

The relative contributions of photoionization and collisional processes (e.g., shocks, heating by cosmic rays) to the physical state of the emission-line gas in NGC 1068 has been a matter of some debate. While Kriss et al. (1992) have attributed the strong C III $\lambda 977$ and N III $\lambda 990$ seen in *HUT* spectra to shock heating, Ferguson et al. (1994) suggest that the strength of these lines result from a combination of continuum fluorescence and dielectronic recombination. Given the importance of continuum scattering to O I $\lambda 1302$, C II $\lambda 1335$ and Mg II $\lambda 2800$, it is not surprising that the same process enhances C III $\lambda 977$ and N III $\lambda 990$. In fact, the recomputed LOWION predicts relatively strong C III $\lambda 977$ and N III $\lambda 990$ (see Table 2). The contribution to both lines from continuum scattering is $\sim 90\%$ for LOWION and $\sim 50\%$ in HIGHION, primarily from zones near the ionized face of the cloud, where the driver lines are optically thin and pumping is most efficient (Ferland 1992). The models predict C III] $\lambda 1909$ /C III $\lambda 977 \approx 5.2$ and N III] $\lambda 1750$ /N III $\lambda 990 \approx 1.1$, compared to 3.15 ± 0.51 and 1.46 ± 0.34 , respectively, from the *HUT* spectra (Kriss et al. 1992), noting that these ratios are quite sensitive to the atomic parameters used in the code. Thus, although we cannot rule out additional heating mechanisms, it is clear that continuum pumping can dramatically enhance these lines in photoionized gas.

Nevertheless, it is interesting to note that turbulent velocities as low as 50 km s^{-1} can fully account for the resonance scattering. The full width at half maximum of C II $\lambda 1335$ is $\sim 1240 \text{ km s}^{-1}$, corrected for Galactic absorption, which indicates that the line is broadened by the summation of different kinematic components. Interestingly, the widths

of the resolved kinematic components of intrinsic UV absorbers in Seyfert 1 galaxies are also typically $\sim 50 \text{ km s}^{-1}$ (Crenshaw et al. 1999). The lack of large scale turbulence implies a lack of violent disruption of the gas.

In KRC, we attributed the large $\text{H}\alpha/\text{H}\beta$ ratio in at least one region to collisional excitation of $\text{H}\alpha$ by an injection of energetic particles, possibly associated with the radio jet, into the NLR gas. This effect was not as apparent in the optical nucleus, and we find no evidence in our STIS data for enhancement of $\text{H}\alpha$ beyond the predictions of the photoionization models. However, there may still be examples of jet/cloud interaction at other locations in the inner NLR OF NGC 1068. This will be addressed in a subsequent paper.

One piece of evidence that heating processes other than photoionization are present is that the electron temperatures predicted by the models are somewhat lower than those estimated from the $[\text{Fe VII}]$. However, the underprediction of the $[\text{Fe VII}]$ ratio is probably due to our assumption that these lines arise in the same gas as the $[\text{O III}]$ lines. Therefore, while it is possible that collisional effects are important in some of the high ionization gas in the inner NLR, most of the observed properties are consistent with photoionization by the central source.

7.3. Geometry of the Inner NLR

While there is no additional evidence to support our proposed geometry for the inner NLR in NGC 1068, assuming that the low ionization gas is screened by a large column absorber resolves a problem with the KRC model regarding the covering factor of the screened gas. Also, it is apparent that conditions in the NLR of NGC 4151 are due to absorption of the ionizing continuum by intervening gas (Alexander et al. 1999; Kraemer et

al. 1999b). If a column of extremely optically thick gas is present, it may have an important effect in the collimation of the ionizing radiation. However, in order to do so, the absorber must have a large covering factor (i.e., 0.5). In addition to NGC 4151, a large column of X-ray absorbing gas has been detected in the Seyfert 1.5, Mrk 6 (Feldmeier et al. 1999), but there are not enough examples to make a statistical determination of the covering factor of the absorber, or its column density as a function of scale-height. Nevertheless, if this component has a large covering factor, it will be important, along with the putative molecular torus and any intrinsic anisotropy of the radiation field, in determining the distribution of ionized gas in the NLR.

8. Conclusions

We have analyzed the STIS UV and optical spectra of the inner nuclear region of NGC 1068, near the optical continuum peak or hot spot. We have constructed photoionization models of the narrow-line gas and have been able to successfully match nearly all the observed dereddened emission-line ratios. From our analysis and modeling of these spectra, we can report the following discoveries regarding the physical conditions near the hot spot.

1. We report the detection of a number of strong coronal emission lines, including [Fe XIV] λ 5303 and [S XII] λ 7611. The latter is the highest ionization UV/optical line ever identified in the NLR of a Seyfert galaxy. The coronal lines are blueshifted with respect to both the systemic velocity of the host galaxy and the lower ionization lines in these spectra. This indicates that the coronal lines arise in a distinct component of narrow-line gas. The lower velocities of other emission-lines may be due to contributions from gas at larger radial distances along our line-of-sight, but it is also possible that much of this gas is co-located with the coronal component, which implies that the velocity of the gas is related to its ionization state and/or density. If this gas is in radial outflow from the nucleus,

these observations may provide important constraints for models of cloud acceleration (the kinematics of the inner NLR of NGC 1068 will be the subject of a later paper).

2. We have used a three-component model to match the narrow emission-line flux ratios, since the kinematics and range of physical conditions clearly indicate that we are sampling distinct emission-line clouds. Most of the high ionization lines, such as C IV $\lambda 1550$, [Ne V] $\lambda 3426$ and [Fe VII] $\lambda 6087$, arise in a component, HIGHION, which is directly ionized by the hidden continuum source and is optically thin at the Lyman limit. Low ionization lines, such as Mg II $\lambda 2800$, [O II] $\lambda 3727$, and [N II] $\lambda 6584$, are formed in a component, LOWION, which is screened from the central source by an optically thick layer of gas ($N_H = 7.4 \times 10^{22} \text{ cm}^{-2}$), similar to that seen in NGC 4151.

Several of the UV resonance lines formed in the low ionization gas (O I $\lambda 1302$, C II $\lambda 1335$, and Mg II $\lambda 2800$) are enhanced by the scattering of continuum radiation. The turbulent velocities required to produce this effect are low, $\sim 50 \text{ km s}^{-1}$. Although this is greater than the thermal velocities within the emitting clouds, it is much less than one might expect if the clouds were being disrupted (e.g., by fast shocks). Also, it is an interesting coincidence that the required turbulent velocities are similar to those measured in the resolved kinematic components of the intrinsic UV absorbers in Seyfert 1s.

Unlike our previous study (KRC), we find no strong evidence for a large overabundance of neon and nitrogen, although the Fe/H ratio in the higher ionization gas appears to be approximately twice solar. Interestingly, there cannot be significant iron enhancement in the low ionization gas, otherwise the model underpredicts the electron temperature in the partially neutral zone. Although iron could be depleted onto dust grains in the neutral gas, we find no evidence of the effects of dust mixed in with the emission-line gas.

Assuming solar abundances, the models underpredict N V $\lambda 1240$ and overpredict N IV] $\lambda 1486$. Resonance scattering and continuum fluorescence cannot sufficiently pump the N V

line to match the observed flux, and, in any case, these processes do not affect the N IV] strength. Although extremely inhomogeneous nitrogen abundances could cause this effect, we think that this is quite unlikely.

3. Although the atomic data is not sufficiently reliable to predict coronal-line flux ratios, we have generated a component, CORONAL, in which all the observed ions are present. Hence, it is plausible that these lines form in photoionized gas. We do not believe that this component is responsible for the scattered continuum radiation, since its covering factor and electron temperature are too low. As such, we postulate that a more highly ionized, co-located component is the scatterer. This component has a covering factor and ionization state similar to the X-ray absorbers detected in Seyfert 1 galaxies.

S.B.K would like to thank Swaraj Tayal, Don Osterbrock, Anand Bhatia, Dick Fisher, and Bruce Woodgate for illuminating conversations about coronal emission-lines. S.B.K. would also like to thank Gary Ferland for useful discussions about resonance scattering and continuum pumping of emission lines. We also thank Cherie Miskey for help with the figures. S.B.K. and D.M.C. acknowledge support from NASA grant NAG 5-4103.

REFERENCES

- Alexander, T., Sturm, E., Lutz, D., Sternberg, A., Netzer, H., & Genzel, R. 1999, *ApJ*, 512, 204
- Allen, C.W. 1977, *Astrophysical Quantities* (London: Univ. of London, Athlone Press)
- Antonucci, R.R., & Miller, J.S. 1985, *ApJ*, 297, 621
- Antonucci, R.R. 1994, *ARA&A*, 31, 64
- Barr, P., White, N.E., Sanford, P.W., & Ives, J.C. 1977, *MNRAS*, 181, 43P
- Bland-Hawthorne, J., Gallimore, J.F., Tacconi, L.J., Brinks, E., Baum, S.A., Antonucci, R.R.J., & Cecil, G.N. 1997, *Ap&SS*, 248, 9
- Capetti, A., Macchetto, F., Axon, D.J., Sparks, W.B., & Boksenberg, A. 1995, *ApJ*, 452, L87
- Capetti, A., Macchetto, F.D., & Lattanzi, M.G. 1997, *Ap&SS*, 248, 127
- Claussen, M.J., & Lo, K.-Y. 1986, *ApJ*, 308, 592
- Crenshaw, D.M., & Kraemer, S.B. 1999, submitted to *ApJ* (Paper I)
- Crenshaw, D.M., Kraemer, S.B., Boggess, A., Maran, S.P., Mushotzky, R.F., & Wu C.-C. 1999, *ApJ*, 516, 750
- Crenshaw, D.M., & Peterson, B.M. 1986, *PASP*, 98, 185
- Durret, F., & Bergeron, J. 1988, *A&AS*, 75 273
- Evans, I.N., Ford, H.C., Kinney, A.L., Antonucci, R.R.J., Armus, L., & Caganoff, S. 1991, *ApJ*, 369, L27
- Feldmeier, J.J., Brandt, W.N., Elvis, M., Fabian, A.C., Iwasaka, K., & Mathur, S. 1999, *ApJ*, 510, 167
- Ferguson, J.W., Ferland, G.J., & Pradhan, A.K. 1991, *ApJ*, 438, L55

- Ferland, G.J., 1992, ApJ, 389, L63
- Ferland, G.J., et al. 1996, ApJ, 461, 683
- Ferland, G.J., et al. 1998, PASP, 110, 761
- Fosbury, R.A.E., & Samsom, A.E. 1983, MNRAS, 204, 1231
- Gallimore, J.F., & Tacconi, L.J. 1997, Ap&SS, 248, 253
- George, I.M., Turner, T.J., Netzer, H., Nandra, K., Mushotzky, R.F., & Yaqoob, T. 1998, ApJS, 114, 73
- Grandi, S.A. 1975a, ApJ, 196, 465
- Grandi, S.A. 1975b, ApJ, 199, L43
- Grandi, S.A. 1978, ApJ, 221, 501
- Greenhill, L.J., & Gwinn C.D. 1997 Ap&SS, 248, 261
- Grevesse, N., & Anders, E. 1989, in AIP Conf. Proc. 183, Cosmic Abundances of Matter, ed. C.J. Waddington (New York: AIP), 1
- Hamann, F., & Korista, K.T. 1996, ApJ, 464, 158
- Halpern, J.P., & Oke, J.B. 1986, ApJ, 301, 753
- Jefferies, J.T., Orrall, F.Q., & Zirker, J.B. 1971, Solar Physics, 16, 103
- Khachikian, E. Ye., & Weedman, D.W. 1971, Astrofizika, 7, 389
- Korista, K.T., & Ferland, G.J. 1989, ApJ, 343, 678
- Koski, A.T., 1978, ApJ, 223, 56
- Kraemer, S.B., Crenshaw, D.M., Hutchings, J.B., Gull, T.R., Kaiser, M.E., Nelson, C.H., Weistrop, D. 1999b, submitted to ApJ
- Kraemer, S.B., Ruiz, J.R., & Crenshaw. D.M. 1998, ApJ, 508, 232 (KRC)

- Kraemer, S.B., Turner, T.J., Crenshaw, D.M., & George, I.M. 1999a, *ApJ*, 519, 69
- Kriss, G.A., et al. 1992, *ApJ*, 394, L37
- Kriss, G.A., et al. 1993, in *Proc, 8th IAP Mtg., First Light in the Universe: Stars or QSO's*, eds. B. Rocca-Volmerange, B. Guideroni, M. Dennefeld, & J. Tran Thanh Van, (Editions Frontieres: Paris) 379
- Krolik, J.H., & Kriss, G.A. 1995, *ApJ*, 447, 512
- Lynds, R. et al. 1991, *ApJ*, 369, L31
- Macchetto, F., Capetti, A., Sparks, W.B., Axon, D.J., & Boksenberg, A. 1994, *ApJ*, 435, L15
- Marshall, F.E., et al. 1993, *ApJ*, 405, 168
- Mason, H.E. 1975, *MNRAS*, 170, 651
- Miller, J.S., & Antonucci, R.R. 1983, *ApJ*, 271, L7
- Miller, J.S., Goodrich, R.W., & Mathews, W.G. 1991, *ApJ*, 378, 47
- Moore, D., Cohen, R.D., & Marcy, G.W. 1996, *ApJ*, 470, 280
- Moorwood, A.F.M., Marconi, A., vander Werf, P.P., & Oliva, E. 1997, *Ap&SS*, 248, 113
- Netzer, H. 1997, *Ap&SS*, 248, 127
- Netzer, H., & Turner, T.J. 1997, *ApJ*, 488, 694
- Nussbaumer, H., & Storey, P.J. 1982, *A&A*, 113, 21
- Oke, J.B., & Sargent, W.L.W. 1968, *ApJ*, 151, 807
- Oliva, E. 1997, in *Emission Lines in Active Galaxies: New Methods and Techniques*, ed. B.M. Peterson, F.-Z. Cheng, & A.S. Wilson (San Francisco: Astronomical Society of the Pacific), ASP Conference Series, 113, 288
- Osterbrock, D.E. 1981, *ApJ*, 246, 696

- Osterbrock, D.E. 1985, *PASP*, 97, 250
- Osterbrock, D.E. 1989, *Astrophysics of Gaseous Nebulae and Active Galactic Nuclei* (Mill Valley, Univ. Science Books)
- Osterbrock, D.E., & Fulbright, J.P. 1996, *PASP*, 108, 183
- Peston, M.V., Fosbury, R.A.E., Boksenberg, A., Mard, M.J., & Wilson, A.S. 1984, *MNRAS*, 208, 347
- Pier, E.A., et al. 1994, *ApJ*, 428, 124
- Reynolds, C.S. 1997, *MNRAS*, 286, 513
- Reynolds, C.S., Ward, M.J., Fabian, A.C., & Celotti, A. 1997, *MNRAS*, 291, 403
- Savage, B.D., & Mathis, J.S. 1979, *ARA&A*, 17, 73
- Seaton, M.J. 1978, *MNRAS*, 185, 5P
- Seyfert, C.K. 1943, *ApJ*, 97, 28
- Tayal, S.S. 1999, in preparation
- Thompson, R.I. 1996, *ApJ*, 459, L61
- Weaver, K.A., Yaqoob, T., Holt, S.S., Mushotzky, R.F., Matsuoka, M., Yamauchi, M. 1994, *ApJ*, 436, L27
- Yaqoob, T., Warwick, R.S., & Pounds, K.A. 1989, *MNRAS*, 236, 153

Fig. 1.— STIS Far-UV (G140L) and Near-UV (G320L), top, Blue Optical (G430L), middle, and Optical/Near-IR (G750L), bottom, spectra of NGC 1068 near the nuclear hot spot.

Fig. 2.— Plot of the recession velocity (cz) against the log of the ionization energy for the emission-line detected in the STIS spectra of the region near the hot spot. As noted in the text, heavily absorbed and severely blended lines have been omitted. The dotted line shows the systemic velocity.

Fig. 3.— Relative brightness profiles of the continuum and [Fe XIV] and [S XII] emission along the slit. Negative positions correspond to the NE direction (see Paper I for the details of the observations).

Fig. 4.— Diagram showing the proposed geometry of the inner NLR of NGC 1068.

Fig. 5.— The ionizing continuum used for the models. The solid line is the absorbed + scattered continuum used for LOWION; the dotted line is the unabsorbed continuum used for HIGHION and CORONAL.

Table 1. NGC 1068 Emission-Line Redshifts and Line Ratios (relative to $H\beta^a$)

	cz^b km s ⁻¹	Ionization Energy (eV) ^c	Observed Ratio	Reddening Corrected ^d
L α λ 1216	1455	13.6	11.54 ± 1.04	30.75 ± 5.65
N V λ 1240	1524	77.4	6.28 ± 0.50	16.19 ± 2.86
O I λ 1302	2028		0.36 ± 0.04	0.84 ± 0.14
C II λ 1335	2316	11.3	0.43 ± 0.12	0.98 ± 0.19
O IV] λ 1402 + (Si IV λ 1398)	1713	77.4	2.34 ± 0.29	4.99 ± 0.74
[Si VIII] λ 1441	1251	246.5	0.25 ± 0.07	0.51 ± 0.10
N IV] λ 1486	969	47.4	0.38 ± 0.08	0.76 ± 0.13
C IV λ 1550	1530	47.9	10.02 ± 0.70	19.83 ± 2.53
He II λ 1640	915	54.4	2.25 ± 0.25	4.34 ± 0.57
C III] λ 1909 + (Si III] $\lambda\lambda$ 1883,1892)	771	24.4	3.52 ± 0.30	7.16 ± 0.96
[Si VII] λ 2148	783	205.1	0.29 ± 0.08	0.76 ± 0.15
C II] λ 2326 (+ O III] λ 2321)	1509	11.3	0.22 ± 0.06	0.47 ± 0.09
[Ne IV] λ 2423	1338	63.5	0.76 ± 0.11	1.44 ± 0.20
[Fe XI] λ 2649	531	262.1	0.49 ± 0.11	0.77 ± 0.13
Mg II λ 2800	1767	7.6	1.32 ± 0.17	1.91 ± 0.21
O III λ 3133	1167	35.1	0.87 ± 0.15	1.13 ± 0.16
He II λ 3204	1452	54.4	0.70 ± 0.20	0.89 ± 0.21
[Ne V] λ 3346	1167	97.1	1.41 ± 0.15	1.74 ± 0.17
[Ne V] λ 3426	1377	97.1	4.05 ± 0.31	4.94 ± 0.36
[Fe VII] λ 3588	1155	100.0	0.39 ± 0.07	0.46 ± 0.07
[O II] λ 3727	1110	13.6	0.48 ± 0.08	0.56 ± 0.08
[Fe VII] λ 3760	1356	100.0	0.74 ± 0.07	0.85 ± 0.07

Table 1—Continued

	cz^b km s ⁻¹	Ionization Energy (eV) ^c	Observed Ratio	Reddening Corrected ^d
[Ne III] λ 3869	1620	41.0	2.07 ± 0.18	2.35 ± 0.19
[Ne III] λ 3967	1542	41.0	0.77 ± 0.10	0.86 ± 0.10
[S II] λ 4072	1590	10.4	0.29 ± 0.05	0.33 ± 0.05
H δ λ 4101	1689	13.6	0.30 ± 0.05	0.33 ± 0.05
H γ λ 4341	1209	13.6	0.62 ± 0.06	0.66 ± 0.06
[O III] λ 4363	1305	35.1	0.40 ± 0.05	0.43 ± 0.05
He II λ 4686	1236	54.4	0.59 ± 0.05	0.60 ± 0.05
H β λ 4861	1320	13.6	1.00	1.00
[O III] λ 4959	1173	35.1	5.02 ± 0.38	4.96 ± 0.38
[O III] λ 5007	1215	35.1	15.39 ± 0.98	15.12 ± 0.98
[Ni XIII] λ 5116 ?	705	352.0	0.06 ± 0.02	0.06 ± 0.02
[Fe VII] λ 5159	999	100.0	0.40 ± 0.04	0.38 ± 0.04
[Fe VI] λ 5176	1755	75.5	0.22 ± 0.03	0.21 ± 0.03
[Fe XIV] λ 5303	708	361.0	0.82 ± 0.06	0.78 ± 0.06
[Ar X] λ 5539 ?	672	422.6	0.15 ± 0.03	0.14 ± 0.03
[Fe VII] λ 5721	1092	100.0	0.92 ± 0.07	0.83 ± 0.07
He I λ 5876	1653	24.6	0.29 ± 0.12	0.25 ± 0.12
[Fe VII] λ 6087	1113	100.0	1.25 ± 0.10	1.08 ± 0.10
[O I] λ 6300 (+ [S III] λ 6312)	720	–	0.32 ± 0.03	0.27 ± 0.03
[Fe X] λ 6374 (+ [O I] λ 6364)	720	235.0	0.95 ± 0.07	0.80 ± 0.07
[N II] λ 6548	1200	14.5	1.18 ± 0.22	0.98 ± 0.22
H α λ 6563	1167	13.6	3.39 ± 0.51	2.81 ± 0.51
[N II] λ 6584	1197	14.5	3.54 ± 0.65	2.94 ± 0.66

Table 1—Continued

	cz^b km s ⁻¹	Ionization Energy (eV) ^c	Observed Ratio	Reddening Corrected ^d
[Ni XV] λ 6702 ?	618	430.0	0.07 ± 0.02	0.06 ± 0.02
[S II] λ 6716	1233	10.4	0.21 ± 0.03	0.17 ± 0.03
[S II] λ 6731	1230	10.4	0.26 ± 0.03	0.21 ± 0.04
[Ar V] λ 7005 ?	1422	59.8	0.18 ± 0.03	0.15 ± 0.03
He I λ 7065	1014	24.6	0.10 ± 0.02	0.08 ± 0.02
[Ar III] λ 7136	1455	27.6	0.37 ± 0.04	0.29 ± 0.05
[O II] λ 7325	1353	13.6	0.30 ± 0.04	0.24 ± 0.04
[S XII] λ 7611	612	504.7	0.47 ± 0.05	0.36 ± 0.05
[Ar III] λ 7751	1590	27.6	0.09 ± 0.02	0.07 ± 0.02
[Fe XI] λ 7892	654	262.1	0.72 ± 0.06	0.55 ± 0.06
[S III] λ 9069	1257	23.3	0.72 ± 0.09	0.51 ± 0.09
[S III] λ 9532	1116	23.3	1.82 ± 0.15	1.28 ± 0.17

^aFlux_{H β} = 18.07 (± 1.11) × 10⁻¹⁵ ergs cm⁻² s⁻¹.

^bcz = 1140 km s⁻¹ for neutral hydrogen in the host galaxy.

^cionization energies from Allen (1968); for blended lines, the ionization energy is for the strongest component.

^dE_{B-V} = 0.17 ± 0.03.

Table 2. Line Ratios from Model Components, Composite, and Observations (relative to $H\beta$)

	HIGHION ^a	LOWION ^{b,c}	Composite ^d	Observed ^e
C III $\lambda 977$	(1.47)	(1.08)	(1.37)	–
N III $\lambda 990$	(0.64)	(0.78)	(0.68)	–
$L\alpha$ $\lambda 1216$	34.18	40.44	35.74	30.17 ± 5.65
N V $\lambda 1240$	3.33	0.00	2.50	16.19 ± 2.86
C II $\lambda 1335$	0.03	0.09 (4.02)	1.01	0.98 ± 0.19
O IV] $\lambda 1402$ + Si IV $\lambda 1398$	4.74	0.00	3.56	4.99 ± 0.19
N IV] $\lambda 1486$	2.99	0.00	2.24	0.76 ± 0.13
C IV $\lambda 1550$	32.52	0.03	24.40	19.83 ± 2.53
He II $\lambda 1640$	6.30	1.29	5.05	4.34 ± 0.57
O III $\lambda 1663$	1.71	0.09	1.31	–
N III $\lambda 1750$	0.81	0.05	0.62	–
C III] $\lambda 1909$ + Si III] $\lambda\lambda 1883,1892$	6.66	1.04	5.25	7.16 ± 0.96
C II] $\lambda 2326$ + O III] $\lambda 2321$	0.24	1.96	0.67	0.47 ± 0.09
[Ne IV] $\lambda 2423$	1.62	0.01	1.22	1.44 ± 0.20
[O II] $\lambda 2470$	0.00	0.77	0.19	–
Mg II $\lambda 2800$	0.00	3.05 (8.54)	2.13	1.91 ± 0.21
He II $\lambda 3204$	0.36	0.08	0.29	0.89 ± 0.21
[Ne V] $\lambda 3346$	1.83	0.00	1.38	1.74 ± 0.17
[Ne V] $\lambda 3426$	4.99	0.00	3.74	4.94 ± 0.36
[Fe VII] $\lambda 3588$	0.46	0.00	0.34	0.44 ± 0.07
[O II] $\lambda 3727$	0.00	2.81	0.70	0.56 ± 0.08
[Fe VII] $\lambda 3760$	0.63	0.00	0.48	0.85 ± 0.07
[Ne III] $\lambda 3869$	1.12	1.67	1.26	2.35 ± 0.19
[Ne III] $\lambda 3967$ + $H\epsilon$	0.50	0.68	0.55	0.86 ± 0.10
[S II] $\lambda 4072$	0.00	0.87	0.22	0.33 ± 0.05
$H\delta$ $\lambda 4100$	0.26	0.26	0.26	0.33 ± 0.05
$H\gamma$ $\lambda 4340$	0.47	0.47	0.47	0.66 ± 0.06

Table 2—Continued

	HIGHION ^a	LOWION ^{b,c}	Composite ^d	Observed ^e
[O III] λ 4363	0.63	0.07	0.49	0.43 ± 0.05
He II λ 4686	0.87	0.19	0.70	0.60 ± 0.05
H β	1.00	1.00	1.00	1.00
[O III] λ 4959	6.60	2.85	5.66	4.96 ± 0.38
[O III] λ 5007	19.80	8.56	16.99	15.12 ± 0.98
[Fe VII] λ 5721	0.79	0.00	0.60	0.83 ± 0.07
He I λ 5876	0.02	0.13	0.05	0.25 ± 0.12
[Fe VII] λ 6087	1.18	0.00	0.88	1.08 ± 0.10
[O I] λ 6300 + [S III] λ 6312	0.00	2.29	0.57	0.27 ± 0.03
[O I] λ 6364 + [Fe X] λ 6374	1.17	0.71	1.06	0.80 ± 0.07
[N II] λ 6548	0.00	2.65	0.66	0.98 ± 0.22
H α λ 6563	2.78	2.94	2.82	2.81 ± 0.51
[N II] λ 6584	0.00	7.65	1.91	2.94 ± 0.66
[S II] λ 6716	0.00	1.03	0.26	0.17 ± 0.03
[S II] λ 6731	0.00	1.22	0.30	0.21 ± 0.04
[O II] λ 7325	0.00	0.98	0.24	0.24 ± 0.04
[S III] λ 9069	0.00	1.17	0.30	0.51 ± 0.09
[S III] λ 9532	0.01	3.08	0.72	1.28 ± 0.17

^a $U = 10^{-1.5}$, $n_H = 6 \times 10^4 \text{ cm}^{-3}$, $N_H = 1 \times 10^{21} \text{ cm}^{-2}$; $\text{Flux}_{H\beta} = 5.06 \text{ ergs cm}^{-2} \text{ s}^{-1}$, emitting area = $1.3 \times 10^{38} \text{ cm}^2$, $F_c = 0.002$.

^b $U = 10^{-3.2}$, $N_H = 3 \times 10^4 \text{ cm}^{-3}$, $N_H = 1 \times 10^{21} \text{ cm}^{-2}$; $\text{Flux}_{H\beta} = 0.25 \text{ ergs cm}^{-2} \text{ s}^{-1}$, emitting area = $8.8 \times 10^{38} \text{ cm}^2$, $F_c = 0.012$.

^cvalues in parenthesis from CLOUDY90, turbulent velocity = 50 km s^{-1} .

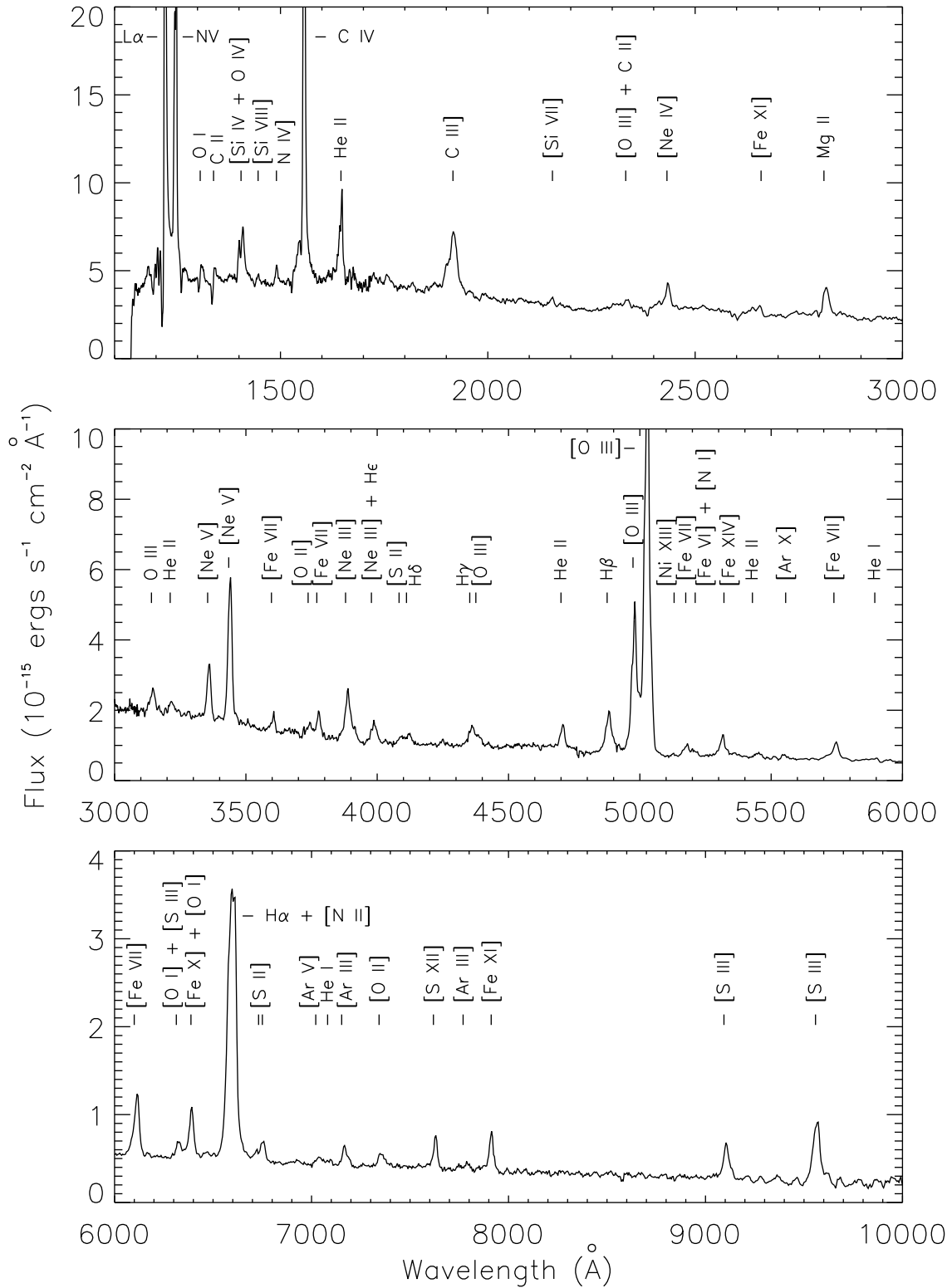
^d75% HIGHION, 25% LOWION.

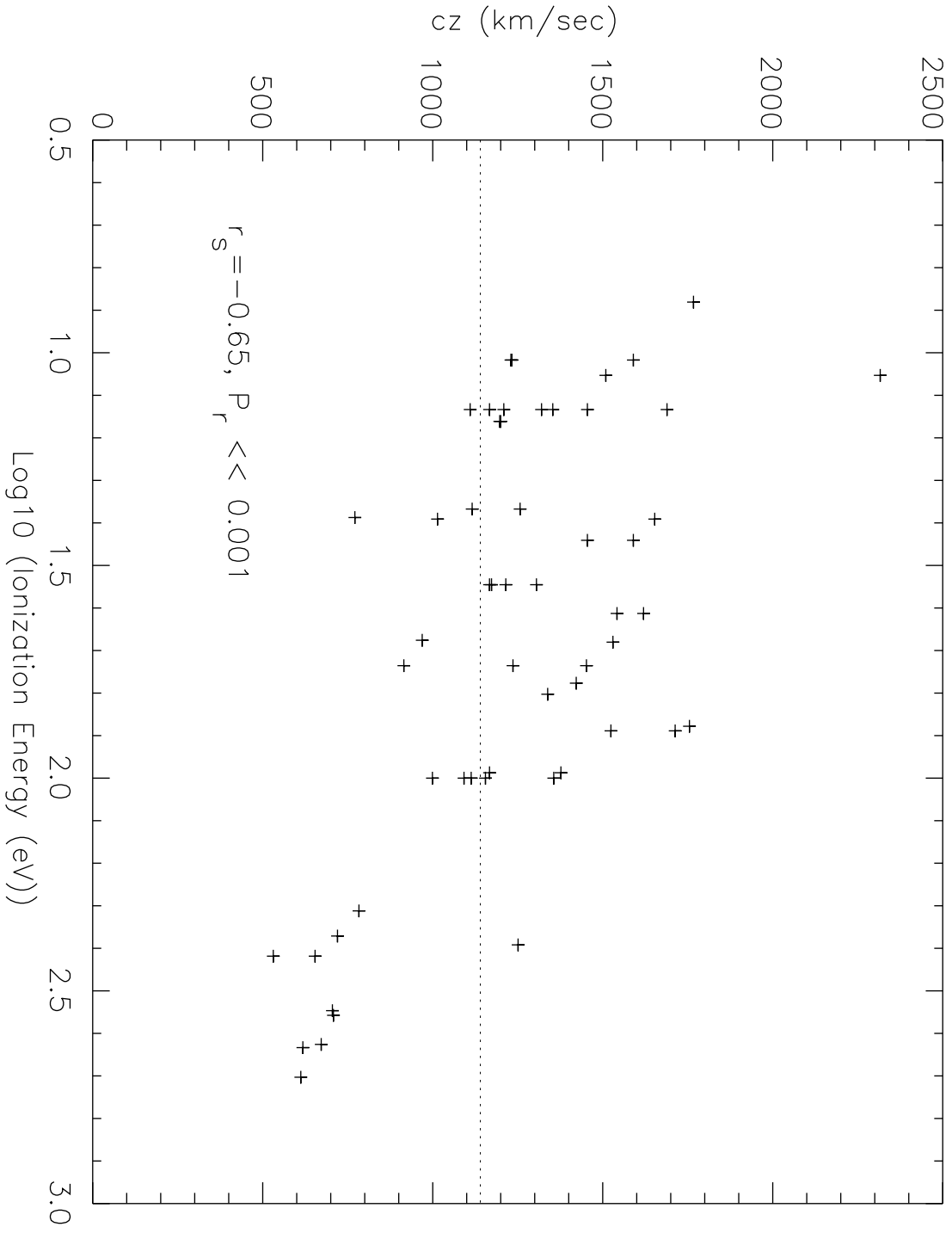
^edereddened; $E_{B-V} = 0.17 \pm 0.03$.

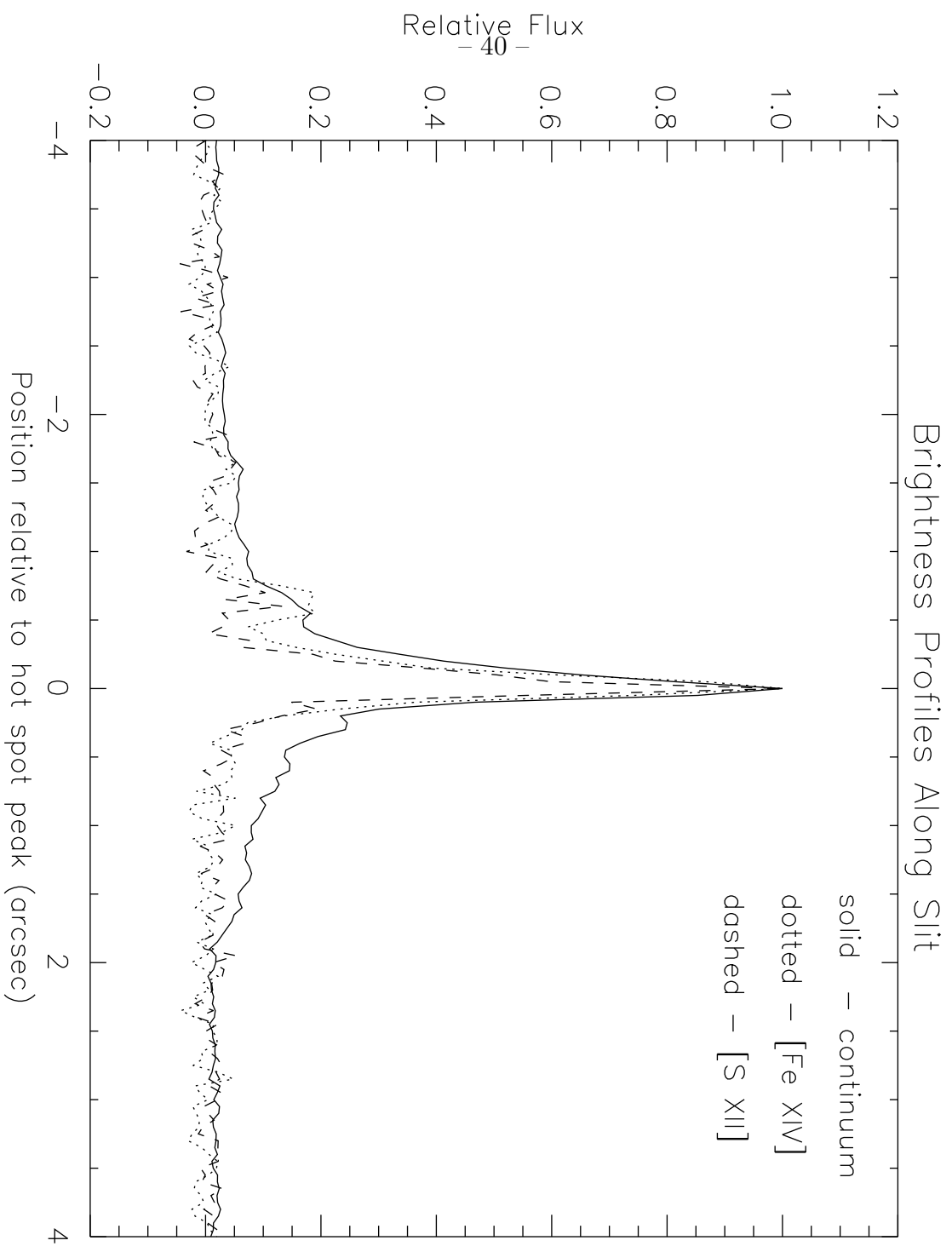
Table 3. Predicted Mean Ionization Fractions (from CORONAL model)

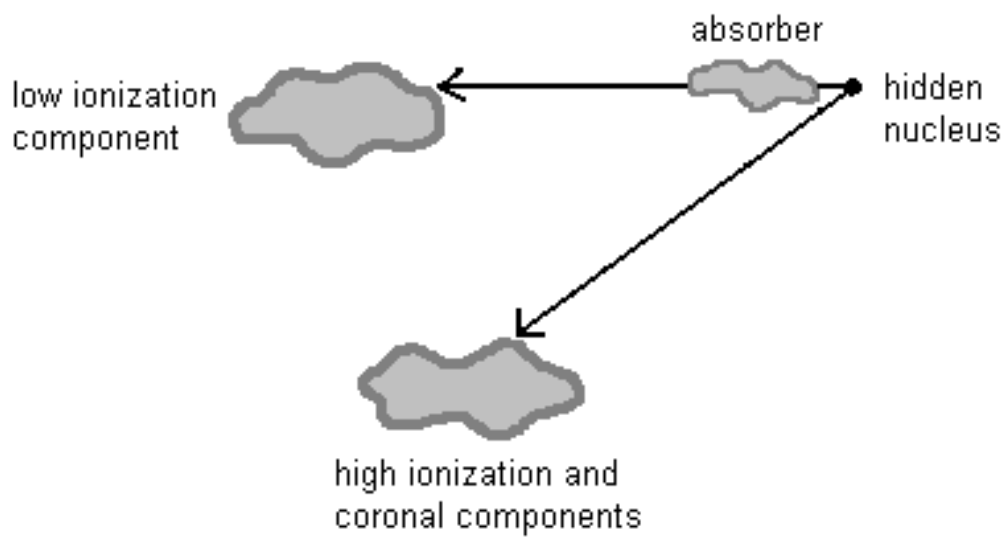
Element	VII	VIII	IX	X	XI	XII	XIII	XIV	XV
Si	0.001 ^a	0.034 ^a	0.191	0.339	0.288	0.099	0.046	0.002	–
S	–	0.019	0.124	0.235	0.261	0.221 ^a	0.107	0.025	0.007
Ar	0.001	0.012	0.101	0.179 ^a	0.229	0.228	0.150	0.077	0.019
Fe	– ^a	–	0.003	0.020 ^a	0.076 ^a	0.188	0.252	0.193 ^a	0.160
Ni	–	–	0.001	0.022	0.106	0.180	0.181 ^a	0.170	0.144 ^a

^aObserved in hot spot spectrum.









observer

